Proposed Valley Valve from Four-Channel Valley Manipulation

Youngjae Kim and J.D. Lee*
Department of Emerging Materials Science, DGIST, Daegu 42988, Korea

(Received 23 May 2018; revised manuscript received 8 January 2019; published 20 March 2019)

Suggesting the *AB*-stacked bilayer WS_2/MoS_2 heterostructure as an ideal architecture for Berry curvature engineering, we theoretically demonstrate that it is possible to manipulate valley polarizations at $\mathbf{K}$ and $-\mathbf{K}$ valleys on each layer in a distinguishable fashion and then attempt an operation using four channels of valley manipulations, that is, four pairwise incorporations of $\mathbf{K}_{WS_2}$ and $(-\mathbf{K})_{WS_2}$, $\mathbf{K}_{MoS_2}$ and $(-\mathbf{K})_{MoS_2}$, $\mathbf{K}_{WS_2}$ and $\mathbf{K}_{MoS_2}$, and $(-\mathbf{K})_{WS_2}$ and $(-\mathbf{K})_{MoS_2}$, within a frame of the electro-optic method. Four-channel valley manipulation, which provokes varied anomalous Lorentz effects, conveys a development of multimode inverse valley Hall currents comprising two intralayer and one interlayer modes, each of which has a different nonlocal resistance. This finding proposes an alternative discipline of valley valve of valleytronics to manage a variable (multilevel) nonlocal resistance to the valley-mediated nonlocal charge current, in analogy with the spin valve of spintronics.

DOI: 10.1103/PhysRevApplied.11.034048

I. INTRODUCTION

In succession to graphene, transition metal dichalcogenides (TMDCs) are promising materials due to various potential functionalities and applications across electronics [1–4], optoelectronics [5–8], spintronics [9,10], topological orders [11,12], and valleytronics. Layered TMDCs, including other two-dimensional systems where the inversion symmetry can be controlled according to their thicknesses, have attracted much attention as base materials for future electronic devices. One of critical interests that these layered systems could deliver will be an alternative internal degree of freedom called the valley degree of freedom. Valley polarizations distinguishable by a strong spin-orbit coupling (SOC) together with the broken inversion symmetry appear as valley degrees of freedom in 2*H*-phase TMDCs and give the spin-valley locking at different crystal momenta $\mathbf{K}$ and $-\mathbf{K}$. Contrasting valley degrees of freedom, which could be selected by the magnetic circular dichroism, enable a manipulation of the valley magnetization and valley-locked spin magnetic moment of carriers [13–16].

Electrical generation and control of valley degrees of freedom has been one of the challenges. The electrical control of the valley Hall effect in bilayer MoS_2 transistor [17], the electrical generation of valley polarization through spin injection from diluted ferromagnetic semiconductors [18], and more recently, the valley magnetoelectric effect in a strained MoS_2 monolayer [19] have been demonstrated. It was also found that the van der Waals (vdW) bilayer of MoS_2 and WSe_2 makes valley-polarized holes in the WSe_2 layer stable with an ultralong valley lifetime, which gives a significant insight into the device applications of TMDC-based heterostructures [20]. With the spin-mediated nonlocal transport driven in the spin Hall effect regime [21], the flavor currents have been measured to show the giant nonlocal response by lifting the spin (and valley) degeneracy in the stripe Hall bar geometry of graphene or bilayer graphene [22–24]. This strongly implies, except for graphene, diverse ramifications of nonlocal transports using the valley Hall effect or the inverse valley Hall effect in TMDCs. Recently, assisted by an additional layer degree of freedom, an attempt to obtain a rich topological phase diagram has been made [25]. The idea of adding the layer degree of freedom may be explored in the valley manipulation.

We suggest a model of the *AB*-stacked bilayer WS_2/MoS_2 heterostructure and devise an alternative strategy of four-channel valley manipulation with which we investigate the valley-mediated nonlocal charge transports. According to the electronic structure of the bilayer WS_2/MoS_2 heterostructure, the excitation energies of $\mathbf{K}_{WS_2}$ and $(-\mathbf{K})_{MoS_2}$ valleys are noted to be about the same and both the valleys can be excited by a single right-circularly polarized (RCP) optical pumping. Likewise, both valleys of $(-\mathbf{K})_{WS_2}$ and $\mathbf{K}_{MoS_2}$ can be excited by a single left-circularly polarized (LCP) optical pumping. In the Hall bar geometry of the heterostructure with four-channel pairwise coordination of valley polarizations, that is, $\mathbf{K}_{WS_2}$ and $(-\mathbf{K})_{WS_2}$, $\mathbf{K}_{MoS_2}$ and $(-\mathbf{K})_{MoS_2}$, $\mathbf{K}_{WS_2}$ and $\mathbf{K}_{MoS_2}$, and $(-\mathbf{K})_{WS_2}$ and $(-\mathbf{K})_{MoS_2}$, we could manage the valley Hall effects in terms of the bias electric

*jdlee@dgist.ac.kr

fields and induce the inverse valley Hall effect leading to the valley-mediated nonlocal charge currents with nonlocal resistances that are variable at multiple levels. This introduces an alternative concept of valley valve, analogous to spin valve, to regulate variable resistances to the spin current in spintronics.

II. RESULTS AND DISCUSSION

Our model of the bilayer WS_2/MoS_2 heterostructure is schematically shown in Fig. 1(a). We focus on the dynamics of holes rather than electrons because holes will be more stable carriers and better at protecting their valley polarizations. In Fig. 1(b), in the bilayer, the signs of the Berry curvature for four-hole valleys of $\mathbf{K}_{WS_2}$, $(-\mathbf{K})_{MoS_2}$, $(-\mathbf{K})_{WS_2}$, and $\mathbf{K}_{MoS_2}$ are indicated as $+, +, -,$ and $-$, respectively, which signifies that the heterostructure is an ideal platform for Berry curvature engineering (shown later). Further in the figure, it is shown that with a single photon energy ω, both the valleys of $\mathbf{K}_{WS_2}$ and $(-\mathbf{K})_{MoS_2}$ are shown to be possibly excited because the MoS_2 band (orange) and WS_2 band (blue) have quite similar gaps in size, that is, 1.73 and 1.68 eV, respectively, according to our first-principles calculation. In addition, it should be noted that the spin structure due to the *AB* stacking would hinder the ultrafast hole transfer from the MoS_2 to the WS_2 layer [26] (see the Fig. S1 of Supplemental Material [27]), in other words, the opposite spin configuration (also different signs of the Berry curvature) between the two layers at the same crystal momentum $\mathbf{K}$ or $-\mathbf{K}$ protects the polarizations of valley holes from the small-momentum scattering. Figure 1(c) gives results of $|\langle\psi_{CB}(\tau=0)|\psi_{VB}(\tau)\rangle|^2$ proportional to the number of optically generated holes, which, in fact, illustrates that a single circularly polarized light with a photon energy of 1.71 eV corresponding to an average band gap could give rise to almost a resonance in both the WS_2 and MoS_2 layers [30]. CB and VB mean the lowest conduction band and the highest valence band of WS_2 or MoS_2, respectively. A slight difference between dipole matrix elements leads to the number of excited holes in WS_2 being a bit larger than that of MoS_2. Note that the $|\psi_{VB(CB)}(\tau)\rangle$ is a time-evolving Kohn-Sham wave function obtained by the first-principles time-dependent density functional theory (TDDFT), whereas $|\psi_{VB(CB)}(\tau=0)\rangle$ is the eigenstate of the system playing the role of the basis.

Considering the Hall bar geometry of the WS_2/MoS_2 heterostructure depicted in Fig. 2(a), we assume that RCP and LCP optical pumpings are applied to the terminals labeled α and β at both ends of the geometry. In terminal α under the optical pumping by a RCP pulse whose vector potential has a Gaussian envelope such as $A(\tau)=A_{RCP}e^{-\tau^2/\tau_W^2}(\cos\omega\tau\hat{\mathbf{x}}-\sin\omega\tau\hat{\mathbf{y}})$ with its optical field strength F_{RCP} $(=\omega A_{RCP})$ and $\tau_W=7.6$ fs, up-spin holes at $\mathbf{K}$ in WS_2 and $-\mathbf{K}$ in MoS_2 could be selectively generated by the circular dichroism. Similarly, in terminal β by a LCP pulse with $F_{LCP}(=\omega A_{LCP})$, down-spin holes at $\mathbf{K}$ in MoS_2 and $-\mathbf{K}$ in WS_2 could be selectively generated. Although the electron-hole pairs are, in fact, excited by the RCP or LCP optical pumping, we keep track of only

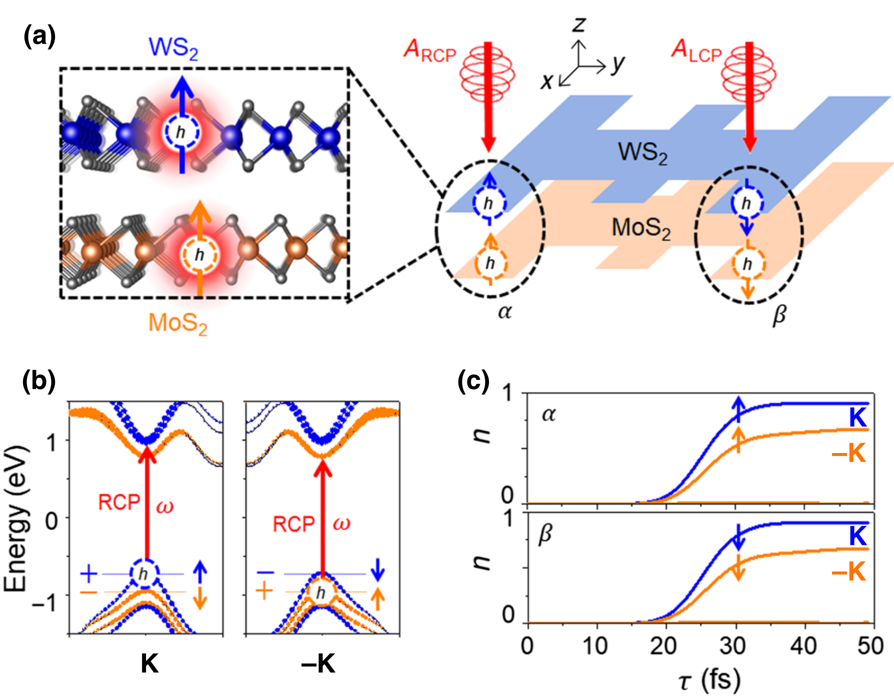

FIG. 1. Schematic description of the Hall bar of WS_2/MoS_2 heterostructure. (a) Optical hole injection using the circular dichroism at both ends of the bar. (b) WS_2 (blue)- and MoS_2 (orange)-dominated electronic bands. In terminal α of the Hall bar, by the RCP optical pumping with a suitable photon energy ω (in fact, 1.71 eV), holes with up spins at crystal momenta $\mathbf{K}$ of WS_2 and $-\mathbf{K}$ of MoS_2 are simultaneously created. $+$ and $-$ denote the signs of the Berry curvature and arrows indicate the spin directions. Similarly, in terminal β of the Hall bar, by the LCP optical pumping, holes with down spins at $-\mathbf{K}$ of WS_2 and $\mathbf{K}$ of MoS_2 are simultaneously created. (c) Calculations of $|\langle\psi_{CB}(\tau=0)|\psi_{VB}(\tau)\rangle|^2$, proportional to the number of injected up-spin holes by the RCP pumping (terminal α) or down-spin holes by the LCP pumping (terminal β), are given as a function of time.

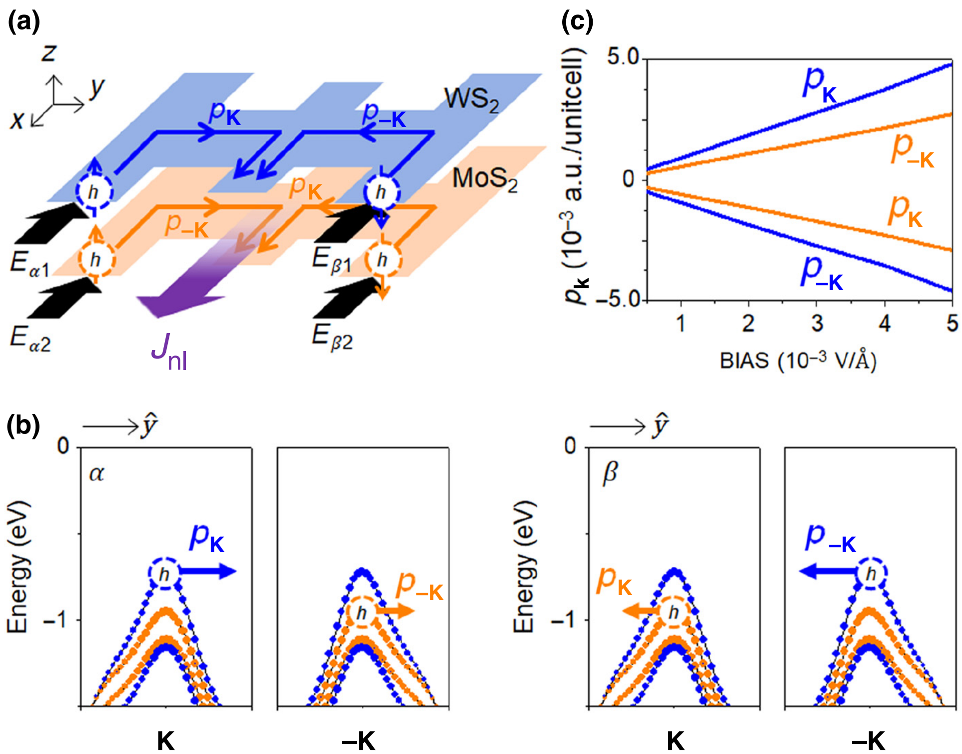

FIG. 2. Schematics of operation of the nonlocal device of the WS_2/MoS_2 heterostructure. (a) Bias electric fields $E_{\alpha1}$, $E_{\alpha2}$, $E_{\beta1}$, and $E_{\beta2}$ induce drift motions of holes optically generated at terminals α and β through the valley Hall effect. $\mathbf{p_K}$ and $\mathbf{p_{-K}}$ represent the hole momenta at the valence band extrema, that is, at the **K** and **−K** valleys, respectively. Note that only holes remain in the Hall bar geometry under our consideration, whereas the electrons are totally escaped from the Hall bar (i.e., by the applied bias fields). (b) Momentum directions are indicated to be different between α terminals and β because of different signs of the Berry curvatures. (c) Momentum expectation values with respect to the in-plane bias field where a.u. is the atomic unit. Blue and orange lines denote WS_2 and MoS_2, respectively.

holes and attempt to manipulate these rather than electrons because holes have more advantages for retaining the valley polarization [31]. $\mathbf{K}_{WS_2}$ and $(-\mathbf{K})_{MoS_2}$ valley holes excited in terminal α feel the Berry curvature with the same sign due to the *AB* stacking of the heterostructure. So do $(-\mathbf{K})_{WS_2}$ and $\mathbf{K}_{MoS_2}$ valley holes in terminal β. As displayed in Fig. 2(a), generated holes can be immediately driven into drift motions via the valley Hall effect according to an application of the in-plane bias electric fields $E_{\alpha1}$, $E_{\alpha2}$, $E_{\beta1}$, and $E_{\beta2}$. Valley hole drifts can be actually estimated from the calculation of hole momenta $\mathbf{p_K}$ and $\mathbf{p_{-K}}$ from $\langle\psi_{VB}^{WS_2}(\mathbf{K},\tau)|\hat{\mathbf{p}}|\psi_{VB}^{WS_2}(\mathbf{K},\tau)\rangle$ and $\langle\psi_{VB}^{MoS_2}(-\mathbf{K},\tau)|\hat{\mathbf{p}}|\psi_{VB}^{MoS_2}(-\mathbf{K},\tau)\rangle$ for WS_2 and MoS_2, respectively. Drifts of valley holes are perpendicular to the bias electric field and are determined by the sign of the Berry curvature through the valley Hall effect, that is,

$$\dot{\mathbf{r}} = \frac{1}{\hbar}\frac{\partial\mathcal{E}(\mathbf{k})}{\partial\mathbf{k}} - \dot{\mathbf{k}}\times\Omega(\mathbf{k}), \qquad (1)$$

where $\mathcal{E}(\mathbf{k})$ is the Bloch band, $\dot{\mathbf{k}}$ is proportional to the bias field, and $\Omega(\mathbf{k})$ is the Berry curvature. The second term is the anomalous Lorentz term, which raises the valley Hall effect. In Fig. 2(b), the drift directions of $\mathbf{K}_{WS_2}$ and $(-\mathbf{K})_{MoS_2}$ valley holes in terminal α and those of $(-\mathbf{K})_{WS_2}$ and $\mathbf{K}_{MoS_2}$ valley holes in terminal β are described. Figure 2(c) provides the hole momenta with respect to the in-plane bias field, which behave like the Ohmic law. The valley Hall conductivity of approximately $\Delta p/\Delta E_{bias}$ of WS_2 is approximately 1.68 times higher than that of MoS_2, which is considered to stem from the difference between WS_2 and MoS_2 in the Berry curvature, that is, with the ratio amounting to approximately 1.57 [32]. Now let us note that four valley holes can be accelerated separately from each other according to an adjusted application of the bias field, that is, a manipulation of a four-bit valley based on $\mathbf{K}_{WS_2}$, $(-\mathbf{K})_{MoS_2}$, $(-\mathbf{K})_{WS_2}$, and $\mathbf{K}_{MoS_2}$ could be achieved beyond the two-bit valley based on **K** and $-$**K** of the usual TMDC monolayers [33]. This is an evident motivation to suggest the WS_2/MoS_2 heterostructure. Drift motions of valley holes from terminals α and β form the valley currents carrying the different valley polarizations and cause a valley neutralization in the center of the geometry of Fig. 2(a). Valley neutralization brings about the inverse valley Hall effect and induces the charge current to flow into a channel in the center of the Hall bar. The charge current is called the nonlocal current J_{nl} because it occurs in the center, but the bias electric fields are applied at both ends. A device using similar nonlocal currents has been discussed in bilayer graphene [23].

The remaining parts of the study are devoted to calculation and discussion of the nonlocal current J_{nl}. Nonlocal transports are calculated based on the flavor fluid model [22] incorporating the first-principles inputs of optically generated hole densities and their Hall conductivities. Then, the nonlocal charge current J_{nl} is given by the following equation (see Fig. S4 [27])

$$J_{\mathrm{nl}}(x) \propto (D_u + D_d)\frac{\sigma_u\sigma_d}{D_u\sigma_u + D_d\sigma_d} \times \exp\left[-\sqrt{\gamma\left(\frac{D_u}{\sigma_u}+\frac{D_d}{\sigma_d}\right)}x\right], \tag{2}$$

where D_u and D_d are the densities of states of two distinct flavor holes (here, u and d should actually mean the sign of the Berry curvature). x is the distance from the terminal (α or β) to the channel in the center of the Hall bar and γ is the flavor relaxation rate. σ_u and σ_d are the conductivities of holes and are given by the relations $\sigma_u \propto p_u n_u$ and $\sigma_d \alpha p_d n_d$. Here, p_u and p_d are the momentum expectation values [Fig. 2(c)] determined by the Berry curvature and bias fields and n_u and n_d are the densities of optically generated holes.

The four-channel valley manipulation (i.e., reduced from the four-bit valley manipulation) requires an exquisite control of in-plane bias electric fields. In this case, according to a control of in-plane bias fields, there could be different modes of operation of the nonlocal valley device as shown in Figs. 3 and 4. In Figs. 3(a)–3(c), J_{nl} is induced wholly in the WS_2 layer from the inverse valley Hall effect by turning on only the biases $E_{\alpha 1}$ and $E_{\beta 1}$ and is calculated from $(\mathbf{p_K} n_\mathbf{K})_{WS_2}$ $(=\sigma_u)$ and $(\mathbf{p_{-K}} n_{-\mathbf{K}})_{WS_2}$ $(=\sigma_d)$ on the basis of Eq. (2), while in Figs. 3(d)–3(f), J_{nl} is wholly in the MoS_2 layer by turning on only the biases $E_{\alpha 2}$ and $E_{\beta 2}$ and from $(\mathbf{p_{-K}} n_{-\mathbf{K}})_{MoS_2}$ and $(\mathbf{p_K} n_\mathbf{K})_{MoS_2}$. In Figs. 3(b) and 3(e), J_{nl} is provided as a function of optical field strengths and bias electric fields symmetrically applied at the terminals α and β. According to Figs. 3(c) and 3(f), a valley neutral condition will be satisfied along the diagonal lines of the figures and results in the extremum of J_{nl}. This can be understood by observing

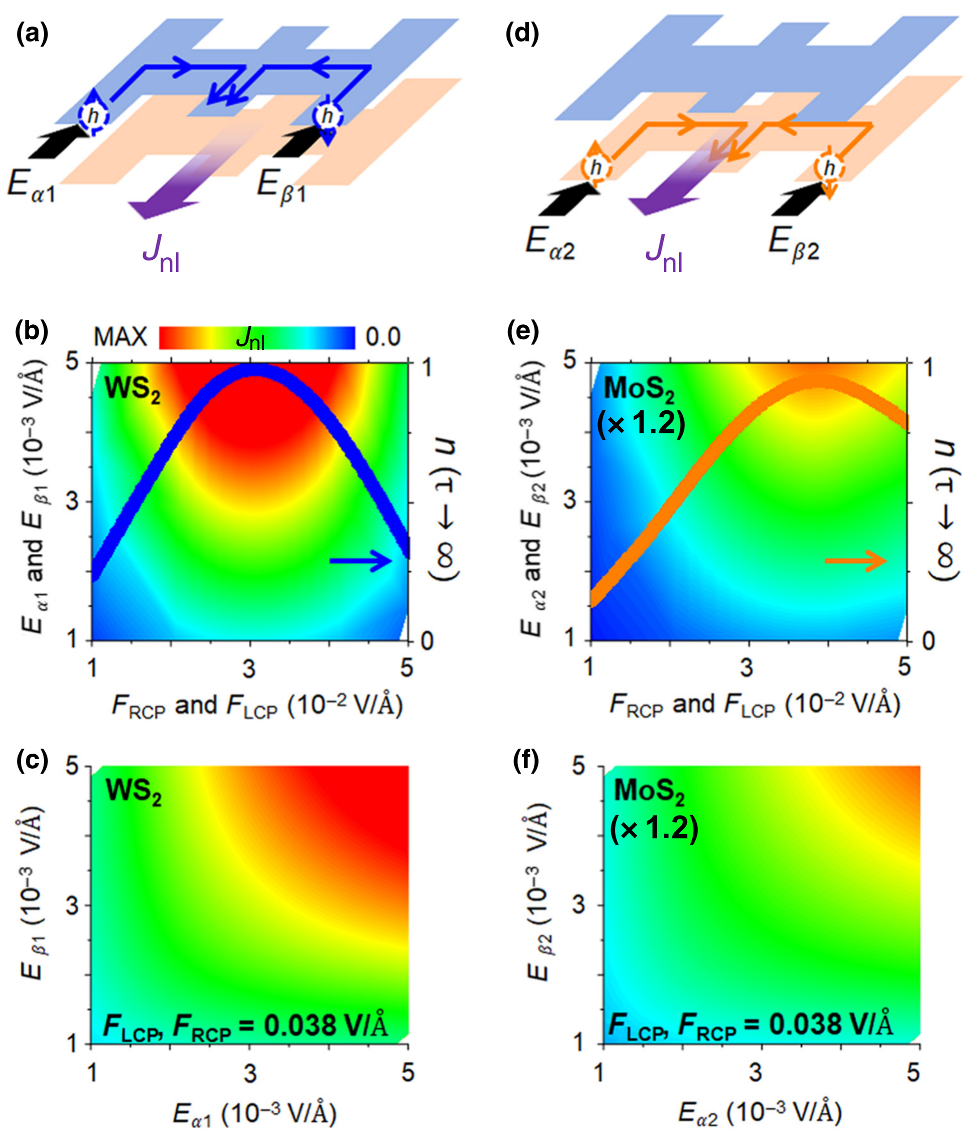

FIG. 3. Nonlocal current J_{nl}. (a)–(c) Nonlocal current is induced by the inverse valley Hall effect in the WS_2 layer and (d)–(f) in the MoS_2 layer, respectively. (b),(e) Nonlocal current as a function of optical field strengths and bias electric fields symmetrically applied at α terminals and β. Blue and orange lines denote the number of excited holes. Nonlocal current is shown to be maximized at the largest number of generated holes at the optical field strengths of approximately 0.03 and approximately 0.038 V/Å. (c),(f) Nonlocal current as a function of bias fields at terminals α and β for fixed optical field strengths of F_{RCP} and F_{LCP}, that is, $F_{\mathrm{RCP}} = F_{\mathrm{LCP}} = 0.038$ V/Å.

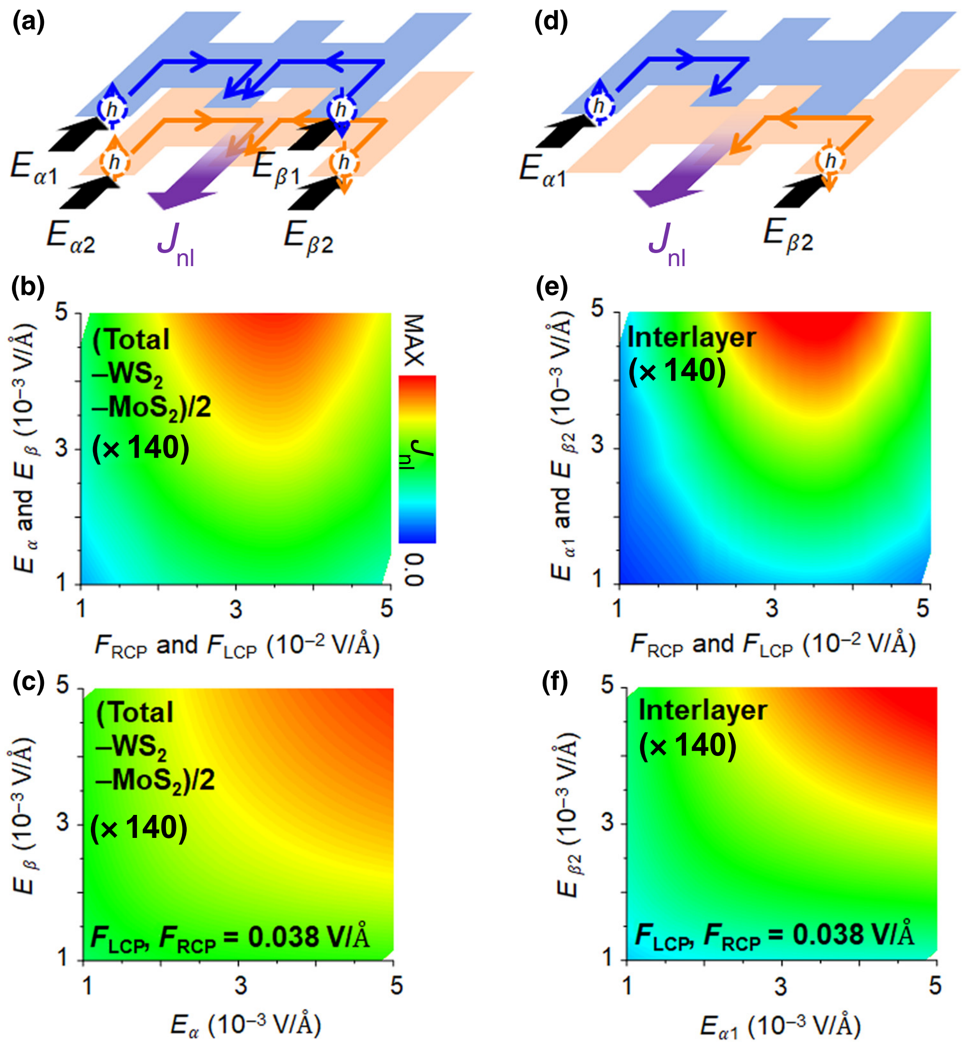

FIG. 4. Interlayer nonlocal current J_{nl}. (a) Nonlocal current J_{nl}^{total} induced by the inverse valley Hall effect in both of the WS_2 and MoS_2 layers. (b),(c) Remnant current of $(J_{nl}^{total} - J_{nl}^{WS_2} - J_{nl}^{MoS_2})/2$ with respect to bias electric fields and optical field strengths. $J_{nl}^{WS_2}$ and $J_{nl}^{MoS_2}$ are from results of Figs. 3(a)–3(c) and Figs. 3(d)–3(f), that is, in the WS_2-intralayer and MoS_2-intralayer modes, respectively. (d) Anomalous mode of the nonlocal current, that is, the interlayer-mode nonlocal current induced by the inverse valley Hall effect between the two layers by turning on the biases $E_{\alpha1}$ and $E_{\beta2}$. (e),(f) Interlayer nonlocal current as a function of bias electric fields and optical field strengths.

that an unbalance of valley holes leads to a sink of the valley current [22]. Comparing the currents between that in the WS_2 layer and that in the MoS_2 layer, the current in the WS_2 layer is shown to be larger than that in the MoS_2 layer by about 50% because of a larger Hall conductivity.

Figure 4(a) indicates the nonlocal current J_{nl}^{total} induced in both of the two layers by turning on all the bias fields, $E_{\alpha1}$, $E_{\beta1}$, $E_{\alpha2}$, and $E_{\beta2}$, that is, obtained from $(\mathbf{p_K} n_\mathbf{K})_{WS_2} + (\mathbf{p_{-K}} n_{-\mathbf{K}})_{MoS_2}$ and $(\mathbf{p_{-K}} n_{-\mathbf{K}})_{WS_2} + (\mathbf{p_K} n_\mathbf{K})_{MoS_2}$. It is interesting to note that the nonlocal current J_{nl}^{total} from both of the layers is always larger than the sum of two intralayer-mode nonlocal currents $J_{nl}^{WS_2}$ and $J_{nl}^{MoS_2}$. The remnant current of $(J_{nl}^{total} - J_{nl}^{WS_2} - J_{nl}^{MoS_2})/2$ with respect to bias electric fields and optical field strengths is shown in Figs. 4(b) and 4(c), whose magnitude is approximately 1% of $J_{nl}^{WS_2}$ or$J_{nl}^{MoS_2}$. A natural physical interpretation of the remnant current would be an anomalous mode of the nonlocal current induced by the inverse valley Hall effect between the two layers by turning on the biases $E_{\alpha1}$ and $E_{\beta2}$ or $E_{\alpha2}$ and $E_{\beta1}$ [Fig. 4(d)]. In this anomalous case, the current is, in fact, tiny because of the interlayer interaction incorporating the Thomas-Fermi-type screening $\propto e^{-\kappa z_0}$ between holes and the p electrons of sulfurs. z_0 is the interlayer distance, that is, 6.47 Å between the W and Mo atoms and κ is the screening constant estimated to be 0.74 Å^{-1} from 0.76 p sulfur electrons per unit cell (see Fig. S5 [27]). The interlayer-mode nonlocal current J_{nl}^{inter} can be calculated directly from the geometry of Fig. 4(d) and the results are provided as a function of bias fields and optical field strengths in Figs. 4(e) and 4(f). An agreement between Figs. 4(b), 4(c), 4(e), and 4(f) is found to be moderately good not only qualitatively but also quantitatively, which firmly supports the physical interpretation of the remnant current.

In Fig. 5, the characteristic *I-V* curves of the nonlocal device of the bilayer WS_2/MoS_2 Hall bar are demonstrated, which shows that the three modes of operation of Figs. 3(a), 3(d), and 4(d) result in three distinct levels of nonlocal resistance such as low (LR), medium (MR), and high resistance (HR), which correspond to the WS_2-intralayer, MoS_2-intralayer, and interlayer modes,

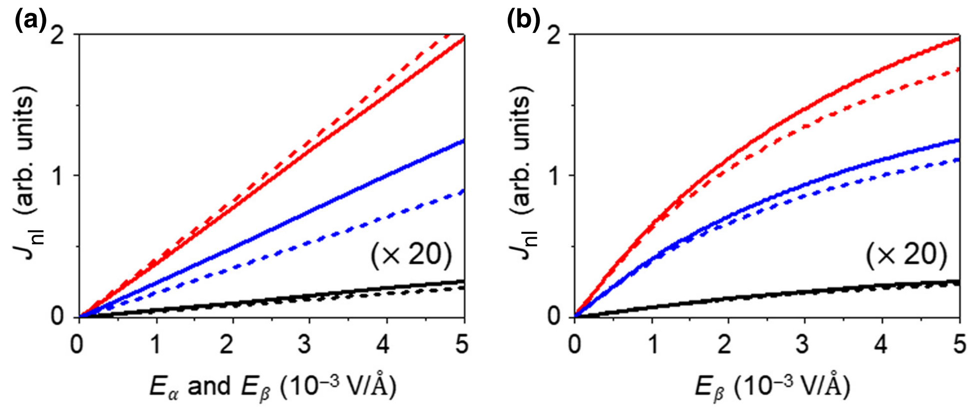

FIG. 5. Characteristic *I-V* curve of the WS_2/MoS_2 heterostructure device. (a) Nonlocal current J_{nl} as a function of bias fields symmetrically applied at terminals α and β, that is, $E_\alpha = E_\beta$, which shows the linear Ohmic behavior. Optical field strengths (keeping $F_{RCP} = F_{LCP}$) are given as 0.038 V/Å (solid line) and 0.025 V/Å (dashed line). (b) Nonlocal current as a function of the bias field E_β at a fixed optical field strength of 0.038 V/Å and fixed bias fields E_α of 0.005 V/Å (solid line) and 0.004 V/Å (dashed line). In the figures, red, blue, and black lines represent LR, MR, and HR modes, respectively, that is, nonlocal current induced in the WS_2-intralayer, MoS_2-intralayer, and interlayer modes.

respectively. In particular, under a condition to guarantee the valley neutralization as displayed in Fig. 5(a), the Ohmic behavior of J_{nl} is clearly obtained and the purely neutralized charge current will be predictable just as in classical electronics. Being deviated from the valley neutralization, the unconventional *I-V* curve, but not the Ohmic behavior, is observed in Fig. 5(b). Even in this case, however, *I-V* curves come out at three distinct levels of resistance. We finally remark that Figs. 3 and 4 suggest an alternative mechanism to manipulate the nonlocal charge resistance in multiple levels by controlling valley-hole motions combinationally in terms of tuning the bias fields. In the apparent functionality, this is highly analogous to the spin valve, a fundamental spintronic device to manipulate the magnetoresistance in terms of controlling the magnetic structure [34]. Hence, it is now proposed that the bilayer WS_2/MoS_2 heterostructure should be an alternative valleytronic device called the valley valve with ternary output channels. It is the *I-V* curves of Fig. 5 that characterize the performance of the ternary valley valve.

III. CONCLUSION

To summarize, suggesting a theoretical model of the *AB*-stack-architectured bilayer WS_2/MoS_2 heterostructure, we investigate a manipulation of four-hole valleys, that is, $\mathbf{K}_{WS_2}$, $(-\mathbf{K})_{MoS_2}$, $(-\mathbf{K})_{WS_2}$, and $\mathbf{K}_{MoS_2}$, which consists of the four-channel valley manipulation (i.e., a reduced version of the four-bit valley manipulation) and the valley-mediated nonlocal charge transports. Holes could be simultaneously created both in $\mathbf{K}_{WS_2}$ and $(-\mathbf{K})_{MoS_2}$ valleys with the RCP optical pumping and similarly, holes in $(-\mathbf{K})_{WS_2}$ and $\mathbf{K}_{MoS_2}$ valleys with the LCP optical pumping. In the Hall bar geometry of the heterostructure, diverse manipulations of those four-hole valleys are possible in terms of a combinational tuning of bias fields, which induces varied inverse valley Hall effects and results in multimode (two intralayer and one interlayer modes) nonlocal charge currents with variable resistances. Thus, we propose an alternative valleytronic device called the valley valve, which materializes the nonlocal resistance at multiple levels in terms of bias fields and is analogous to the spin valve of spintronics. A valley valve with the four-channel valley manipulation based on the Berry curvature engineering will open possibilities for the advancement of valleytronics using two-dimensional materials.

ACKNOWLEDGMENTS

This work was supported by the Basic Science Research Program (Grant No. 2016R1A2B4013141) through the National Research Foundation of Korea (NRF) and also by the DGIST R&D Programs (Grants No. 18-BD-0403 and No. 18-BT-02) funded by the Ministry of Science and ICT.

[1] K. F. Mak, C. Lee, J. Hone, J. Shan, and T. F. Heinz, Atomically Thin MoS_2: A New Direct-Gap Semiconductor, Phys. Rev. Lett. **105**, 136805 (2010).

[2] R. Ganatra and Q. Zhang, Few-layer MoS_2: A promising layered semiconductor, ACS Nano **8**, 4074 (2014).

[3] M. M. Ugeda, A. J. Bradley, S.-F. Shi, F.-H. da Jornada, Y. Zhang, D. Y. Qiu, W. Ruan, S.-K. Mo, Z. Hussain, Z.-X. Shen, F. Wang, S. G. Louie, and M. F. Crommie, Giant bandgap renormalization and excitonic effects in a monolayer transition metal dichalcogenide semiconductor, Nat. Mater. **13**, 1091 (2014).

[4] B. Radisavljevic, A. Radenovic, J. Brivio, V. Giacometti, and A. Kis, Single-layer MoS_2 transistors, Nat. Nanotechnol. **6**, 147 (2011).

[5] Y. Yu, Y. Yu, L. Huang, H. Peng, L. Xiong, and L. Cao, Giant gating tunability of optical refractive index in transition metal dichalcogenide monolayers, Nano Lett. **17**, 3613 (2017).

[6] M. S. Kim, S. J. Yun, Y. Lee, C. Seo, G. H. Han, K. K. Kim, Y. H. Lee, and J. Kim, Biexciton emission from edges and grain boundaries of triangular WS_2 monolayers, ACS Nano **10**, 2399 (2016).

[7] G. Wang, X. Marie, B. L. Liu, T. Amand, C. Robert, F. Cadiz, P. Renucci, and B. Urbaszek, Control of Exciton Valley Coherence in Transition Metal Dichalcogenide Monolayers, Phys. Rev. Lett. **117**, 187401 (2016).

[8] G. Wang, C. Robert, M. M. Glazov, F. Cadiz, E. Courtade, T. Amand, D. Lagarde, T. Taniguchi, K. Watanabe, B. Urbaszek, and X. Marie, In-Plane Propagation of Light in Transition Metal Dichalcogenide Monolayers: Optical Selection Rules, Phys. Rev. Lett. **119**, 047401 (2017).

[9] Z. Wang, L. Zhao, K. F. Mak, and J. Shan, probing the spin-polarized electronic band structure in monolayer transition metal dichalcogenides by optical spectroscopy, Nano Lett. **17**, 740 (2017).

[10] X. Chen, T. Yan, B. Zhu, S. Yang, and X. Cui, Optical control of spin polarization in monolayer transition metal dichalcogenides, ACS Nano **11**, 1581 (2017).

[11] X. F. Qian, J. W. Liu, L. Fu, and J. Li, Quantum spin Hall effect in two-dimensional transition metal dichalcogenides, Science **346**, 1344 (2014).

[12] Y. Ma, L. Kou, X. Li, Y. Dai, and T. Heine, Two-dimensional transition metal dichalcogenides with a hexagonal lattice: Room-temperature quantum spin Hall insulators, Phys. Rev. B **93**, 035442 (2016).

[13] H. Zeng, J. Dai, W. Yao, D. Xiao, and X. Cui, Valley polarization in MoS_2 monolayers by optical pumping, Nat. Nanotechnol. **7**, 490 (2012).

[14] T. Cao, G. Wang, W. Han, H. Ye, C. Zhu, J. Shi, Q. Niu, P. Tan, E. Wang, B. Liu, and J. Feng, Valley-selective circular dichroism of monolayer molybdenum disulphide, Nat. Commun. **3**, 887 (2012).

[15] X. Xu, W. Yao, D. Xiao, and T. F. Heinz, Spin and pseudospins in layered transition metal dichalcogenides, Nat. Phys. **10**, 343 (2014).

[16] J. Kim, X. Hong, C. Jin, S.-F. Shi, C.-Y. S. Chang, M.-H. Chiu, L.-J. Li, and F. Wang, Ultrafast generation of pseudo-magnetic field for valley excitons in WSe_2 monolayers, Science **346**, 1205 (2014).

[17] J. Lee, K. F. Mak, and J. Shan, Electrical control of the valley Hall effect in bilayer MoS_2 transistors, Nat. Nanotechnol. **11**, 421 (2016).

[18] Y. Ye, J. Xiao, H. Wang, Z. Ye, H. Zhu, M. Zhao, Y. Wang, J. Zhao, X. Yin, and X. Zhang, Electrical generation and control of the valley carriers in a monolayer transition metal dichalcogenide, Nat. Nanotechnol. **11**, 598 (2016).

[19] J. Lee, Z. Wang, H. Xie, K. F. Mak, and J. Shan, Valley magnetoelectricity in single-layer MoS_2, Nat. Mater. **16**, 887 (2017).

[20] J. Kim, C. Jin, B. Chen, H. Cai, T. Zhao, P. Lee, S. Kahn, K. Watanabe, T. Taniguchi, S. Tongay, M. F. Crommie, and F. Wang, Observation of ultralong valley lifetime in WSe_2/MoS_2 heterostructures, Sci. Adv. **3**, e1700518 (2017).

[21] D. A. Abanin, A. V. Shytov, L. S. Levitov, and B. I. Halperin, Nonlocal charge transport mediated by spin diffusion in the spin Hall effect regime, Phys. Rev. B **79**, 035304 (2009).

[22] D. A. Abanin, S. V. Morozov, L. A. Ponomarenko, R. V. Gorbachev, A. S. Mayorov, M. I. Katsnelson, K. Watanabe, T. Taniguchi, K. S. Novoselov, L. S. Levitov, and A. K. Geim, Giant nonlocality near the dirac point in graphene, Science **332**, 328 (2011).

[23] Y. Shimazaki, M. Yamamoto, I. V. Borzenets, K. Watanabe, T. Taniguchi, and S. Tarucha, Generation and detection of pure valley current by electrically induced Berry curvature in bilayer graphene, Nat. Phys. **11**, 1032 (2015).

[24] M. Sui, G. Chen, L. Ma, W.-Y. Shan, D. Tian, K. Watanabe, T. Taniguchi, X. Jin, W. Yao, D. Xiao, and Y. Zhang, Gate-tunable topological valley transport in bilayer graphene, Nat. Phys. **11**, 1027 (2015).

[25] J. Lu, C. Qiu, W. Deng, X. Huang, F. Li, F. Zhang, S. Chen, and Z. Liu, Valley Topological Phases in Bilayer Sonic Crystals, Phys. Rev. Lett. **120**, 116802 (2018).

[26] X. Hong, J. Kim, S.-F. Shi, Y. Zhang, C. Jin, Y. Sun, S. Tongay, J. Wu, Y. Zhang, and F. Wang, Ultrafast charge transfer in atomically thin MoS_2/WS_2 heterostructures, Nat. Nanotechnol. **9**, 682 (2014).

[27] See Supplemental Material at http://link.aps.org/supplemental/10.1103/PhysRevApplied.11.034048 for band structure and electronic configuration of *AA*- and *AB*-stacked transition metal dichacogenicde heterostructures (Fig. S1), creation of holes in the WS_2/MoS_2 heterostructure by the circularly polarized lights (Fig. S2), transition (hole creation) probabilities as a function of time (Fig. S3), flavor-fluid model in a Hall bar geometry (Fig. S4), screening effect between WS_2 and MoS_2 layers (Fig. S5).

[28] L. Yuan, T.-F. Chung, A. Kuc, Y. Wan, Y. Xu, Y. P. Chen, T. Heine, and L. Huang, Photocarrier generation from interlayer charge-transfer transitions in WS_2-graphene heterostructures, Sci. Adv. **4**, e1700324 (2018).

[29] D. J. Trainer, A. V. Putilov, C. D. Giorgio, T. Saari, B. Wang, M. Wolak, R. U. Chandrasena, C. Lane, T.-R. Chang, H.-T. Jeng, H. Lin, F. Kronast, A. X. Gray, X. Xi, J. Nieminen, A. Bansil, and M. Iavarone, Inter-layer coupling induced valence band edge shift in mono- to few-layer MoS_2, Sci. Rep. **7**, 40559 (2017).

[30] To perform the first-principles calculation, we employthe time-dependent density functional theory (TDDFT) implemented in the full-potential linearized augmented plane wave (FPLAPW) method within the ELK code. In the TDDFT calculation, the local density approximation (LDA) of the Ceperley-Alder exchange correlation functional based on Perdew-Zunger parameters with SOC, $6\times6\times1$ k point grids, and 9.0 rgkmax are used. All augmented plane waves (APWs) are converted into linearized APWs for the calculation. A lattice constant of the WS_2/MoS_2 heterostructure is 3.14 Å, which is an averaged parameter of 3.15 Å and 3.13 Å of the monolayer WS_2 [28] and MoS_2 [29], respectively.

[31] C. Mai, A. Barrette, Y. Yu, Y. G. Semenov, K. W. Kim, L. Cao, and K. Gundogdu, Many-body effects in valleytronics: Direct measurement of valley lifetimes in single-layer MoS_2, Nano Lett. **14**, 202 (2014).

[32] D. Xiao, G.-B. Liu, W. Feng, X. Xu, and W. Yao, Coupled Spin and Valley Physics in Monolayers of MoS_2 and Other Group-VI Dichalcogenides, Phys. Rev. Lett. **108**, 196802 (2012).

[33] We understand that 1L-MoS_2 could have four distinguishable valley states such as 0, K, −K, and K and −K, which form two bits from "0 and K" (one bit) and "0 and −K" (one bit). The heterostructure of 1L-WS_2 and 1L-MoS_2 could then configure sixteen distinguishable states, corresponding to four bits.

[34] B. Dienny, V. S. Speriosu, S. S. P. Parkin, B. A. Gurney, D. R. Wilhoit, and D. Mauri, Giant magnetoresistive in soft ferromagnetic multilayers, Phys. Rev. B **43**, 1297(R) (1991).